nature catalysis

ARTICLES

https://doi.org/10.1038/s41929-019-0241-7

Promoting nitrogen electroreduction to ammonia with bismuth nanocrystals and potassium cations in water

Yu-Chen Hao[1,5], Yu Guo[2,5], Li-Wei Chen[1], Miao Shu[3], Xin-Yu Wang[2], Tong-An Bu[1], Wen-Yan Gao[1], Nan Zhang[1], Xin Su[1], Xiao Feng[1], Jun-Wen Zhou[1], Bo Wang[1], Chang-Wen Hu[1], An-Xiang Yin[1*], Rui Si[3*], Ya-Wen Zhang[2*] and Chun-Hua Yan[2,4*]

The electrochemical nitrogen reduction reaction (ENRR) can allow the production of ammonia from nitrogen and water under ambient conditions and is regarded as a sustainable alternative to the industrial Haber–Bosch process. However, electrocatalytic systems that selectively and efficiently catalyse nitrogen reduction remain elusive due to the strong competition with the hydrogen evolution reaction. Here, we report a strategy to simultaneously promote ENRR selectivity and activity using bismuth nanocrystals and potassium cations. Bismuth exhibits higher intrinsic ENRR activity than transition metals due to the strong interaction between the Bi 6*p* band and the N 2*p* orbitals. Potassium cations stabilize key nitrogen-reduction intermediates and regulate proton transfer to increase the selectivity. A high Faradaic efficiency of 66% and ammonia yield of 200 mmol g^{-1} h^{-1} (0.052 mmol cm^{-2} h^{-1}) are obtained in aqueous electrolyte under ambient conditions. This strategy represents a general method to expand the library of catalysts and promoters for the selective electrochemical reduction of stable molecules.

The electrochemical nitrogen reduction reaction (ENRR) is a sustainable approach that can produce ammonia from air and water when powered by renewable electricity[1–7]. Unlike the industrial Haber–Bosch process, where hydrogen and nitrogen form ammonia at high temperatures (400–500 °C) and pressures (200–300 atm)[8,9], the ENRR can hydrogenate nitrogen molecules with protons and electrons at ambient temperature and pressure. Despite tremendous efforts in recent decades, electrocatalysts that selectively and efficiently reduce nitrogen to ammonia remain elusive. Most catalysts show a higher overpotential for the ENRR than for the hydrogen evolution reaction (HER)[10,11] and therefore exhibit limited selectivity (up to ~10%) and activity in aqueous solutions due to the critical challenge of overcoming HER competition[12–21].

Previous strategies for promoting the ENRR include modifying transition-metal-based catalysts[16–18] and/or using non-aqueous electrolytes[22–24]. However, these efforts cannot simultaneously realize both high selectivity and activity for ENRR. Theoretical calculations show that the scaling relations between the adsorption energies for ENRR intermediates would make the simultaneous promotion of selectivity and activity a dilemma for transition-metal catalysts[10,11]. Catalysts with theoretically high ENRR activity (located near the top of the volcano plot for ENRR) exhibit very poor selectivity due to strong HER competition. Metals that bind nitrogen more strongly than hydrogen (for example, several early transition metals located at the left side of the volcano plot) would exhibit possible higher ENRR selectivity; however, their ENRR activity is very limited because their binding to nitrogen species is too strong and the desorption of certain intermediates would be very slow[10,11]. Previous reports suggest that non-aqueous solutions can suppress HER by limiting proton concentration[22–24]. However, the lack of proton supply would also limit activity, because ENRR falls into the category of proton-coupled electron transfer (PCET) reactions[6]. As a result, the dilemma for selectivity and activity cannot be resolved by previously proposed strategies, and the ENRR is energetically inefficient and kinetically sluggish in state-of-the-art catalytic systems[1–7]. For possible applications, we thus need to develop novel electrochemical systems that can modulate the reaction thermodynamics and kinetics to selectively and efficiently promote nitrogen reductions.

Here, we report a strategy in which bismuth catalysts and potassium cations both contribute to the ENRR process with high selectivity and activity, simultaneously. Bismuth can offer a lower free-energy change (ΔG) for the potential-determining step (PDS) and thus better intrinsic ENRR activity than typical transition-metal catalysts (for example, Au) (Fig. 1a). Potassium cations can further lower the ΔG required by that PDS (Fig. 1b) and regulate the proton diffusion process to make the reaction more selective to nitrogen reduction (Fig. 1c,d). As a result, the Bi–K^+ pair can promote the ENRR to achieve a record-high Faradaic efficiency (66%) and ammonia yield (200 mmol NH_3 g^{-1} h^{-1}) in aqueous solutions under ambient conditions.

Results

Catalyst synthesis and characterization. Bismuth catalysts of different sizes were prepared using a solvothermal method and supported on carbon black to compare their catalytic properties. Transmission electron microscopy (TEM) and high-resolution

[1]MOE Key Laboratory of Cluster Science, Beijing Key Laboratory of Photoelectronic/Electrophotonic Conversion Materials, School of Chemistry and Chemical Engineering, Beijing Institute of Technology, Beijing, China. [2]Beijing National Laboratory for Molecular Sciences, State Key Laboratory of Rare Earth Materials Chemistry and Applications, PKU-HKU Joint Laboratory in Rare Earth Materials and Bioinorganic Chemistry, College of Chemistry and Molecular Engineering, Peking University, Beijing, China. [3]Shanghai Synchrotron Radiation Facility, Shanghai Institute of Applied Physics, Chinese Academy of Sciences, Shanghai, China. [4]College of Chemistry and Chemical Engineering, Lanzhou University, Lanzhou, China. [5]These authors contributed equally: Yu-Chen Hao and Yu Guo. *e-mail: yin@bit.edu.cn; sirui@sinap.ac.cn; ywzhang@pku.edu.cn; yan@pku.edu.cn

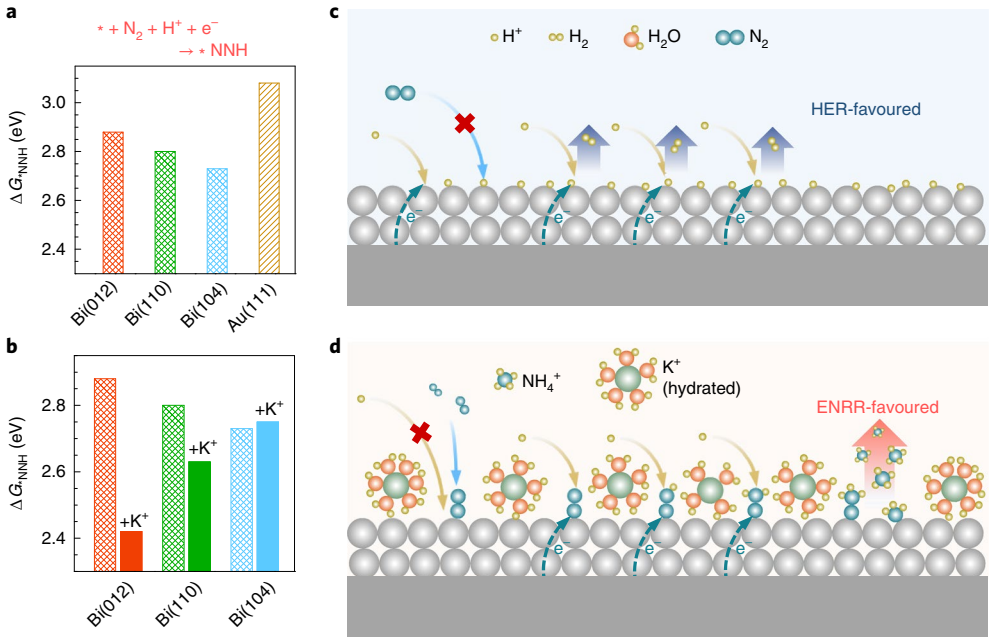

Fig. 1 | Promoting the ENRR with bismuth catalysts and potassium cations. a, The free-energy change (ΔG_{*NNH}) required to form *NNH ($* + N_2 + H^+ + e^- \rightarrow$ *NNH) on Bi (012), (110), (104) and Au (111) facets. **b**, ΔG_{*NNH} on Bi (012), (110) and (104) facets without (patterned bars) and with (filled bars) K^+ cations. **c**,**d**, Mass transfer of protons and nitrogen molecules to the catalyst surface in electrolytes without (**c**) and with (**d**) K^+ cations. **c**, In acidic solutions without K^+ cations, protons can be transferred to the surface readily, and HER will dominate. **d**, K^+ hinders proton transfer to the catalyst surfaces. Nitrogen will be adsorbed preferentially, and the ENRR is promoted.

TEM (HRTEM) images demonstrate that the bismuth nanocrystals (BiNCs) are quasi-spherical polyhedrons with a size distribution of 7.35 ± 1.62 nm (Fig. 2a and Supplementary Fig. 1), the bismuth nanoparticles (BiNPs) exhibit a larger size distribution of 19.43 ± 1.71 nm, while the bismuth bulk particles (BiBPs) are even larger particles (>100 nm) (Supplementary Fig. 2). X-ray diffraction (XRD) patterns confirmed that these as-prepared catalysts crystallized in the rhombohedral phase (space group $R{-}3m$) (Fig. 2c and Supplementary Fig. 2). The HRTEM images also revealed that the BiNCs are enclosed with (012), (110) and (104) surfaces (Fig. 2b and Supplementary Fig. 3). X-ray photoelectron spectroscopy (XPS) profiles showed that the as-obtained BiNCs are composed of zero-valence bismuth elements (Fig. 2d). An in situ X-ray absorption near-edge spectroscopy (XANES) profile also demonstrated that the active species during the electrocatalytic reactions is Bi^0 (Fig. 2f and Supplementary Fig. 4). These results are consistent with the calculated Pourbaix phase diagram of bismuth species (Supplementary Fig. 5), which predicts that Bi(s) is the most thermodynamically stable phase under the present operating conditions.

Electroreduction of N_2 to NH_3. Electrochemical measurements were carried out with a two-compartment cell (H-cell) separated by a proton-exchange membrane (Nafion 115) at room temperature and atmospheric pressure. A platinum plate (1×1 cm^2) and a saturated calomel electrode (SCE) were used as the counter- and reference electrodes, respectively. The working electrode was prepared by dispersing metal catalysts onto a glassy carbon electrode (diameter, 4 mm) with a metal loading of 94 μg cm^{-2} (Supplementary Table 1). Nitrogen/argon was fed into the cathodic electrolyte by gas bubbling during the electrolysis. The produced ammonia was measured with colorimetric assays (Nessler's reagent), enzymatic ammonia assay kits and NMR spectra (Supplementary Figs. 6 and 7). Additional tests were carried out to exclude possible interference from any contaminants. No ammonia could be detected in (1) electrolytes bubbled by air with open circuits for 10 h, (2) electrolytes saturated by N_2 with open circuits for 10 h or (3) argon-saturated solutions electrolysed for 10 h (Supplementary Fig. 8). In addition, only $^{15}NH_4^+$ could be detected by NMR when $^{15}N_2$ was used as the dinitrogen source (Supplementary Fig. 9). Therefore, the ammonia detected during ENRR was exclusively produced by the catalytic electroreduction of nitrogen.

Optimized ENRR performances were obtained in acidic potassium sulfate electrolytes (pH 3.5, 1.0 mol l^{-1} of K^+). According to the linear sweep voltammetry (LSV) curves in Fig. 3a, BiNCs exhibited much higher current densities than BiNPs and BiBPs, and carbon black did not show any observable ammonia production activity. As shown in Fig. 3b,c, ammonia production on BiNCs could be detected at −0.50 V (versus RHE) with an ammonia-producing Faradaic efficiency of 32%. The Faradaic efficiency increased to as high as 67% at −0.60 V with an effective current density (j_N) of 0.50 mA cm^{-2} (5.3 mA mg^{-1}). The effective current density could be further raised to 0.60 mA cm^{-2} at −0.70 V, although the Faradaic efficiency would drop to about 20%. In comparison, BiNPs and BiBPs offered smaller Faradaic efficiencies of 48 and 41% with current densities of 0.16 and 0.066 mA cm^{-2} at –0.60 V, respectively. The estimated turnover frequency (TOF, h^{-1}) values also suggested the higher activity for BiNCs than that on larger BiNPs (Supplementary Table 2). Possible by-products (that is, H_2, N_2H_4) were also quantified (Supplementary Figs. 10 and 11). At −0.60 V, BiNCs exhibited a Faradaic efficiency of 67% for NH_3, 31% for H_2 and 2% for N_2H_4. Further isotope-labelled quantification experiments confirmed that the obtained ammonia was produced from the ENRR exclusively with high Faradaic efficiency (67%) (Supplementary Fig. 9). No significant differences in ENRR performance of BiNCs (LSV, Faradaic efficiency and ammonia evolution rate) could be observed between electrolysis experiments with a platinum plate and a carbon rod as counterelectrode, respectively, excluding the possible contamination of Pt dissolved from the anode (Supplementary Fig. 12).

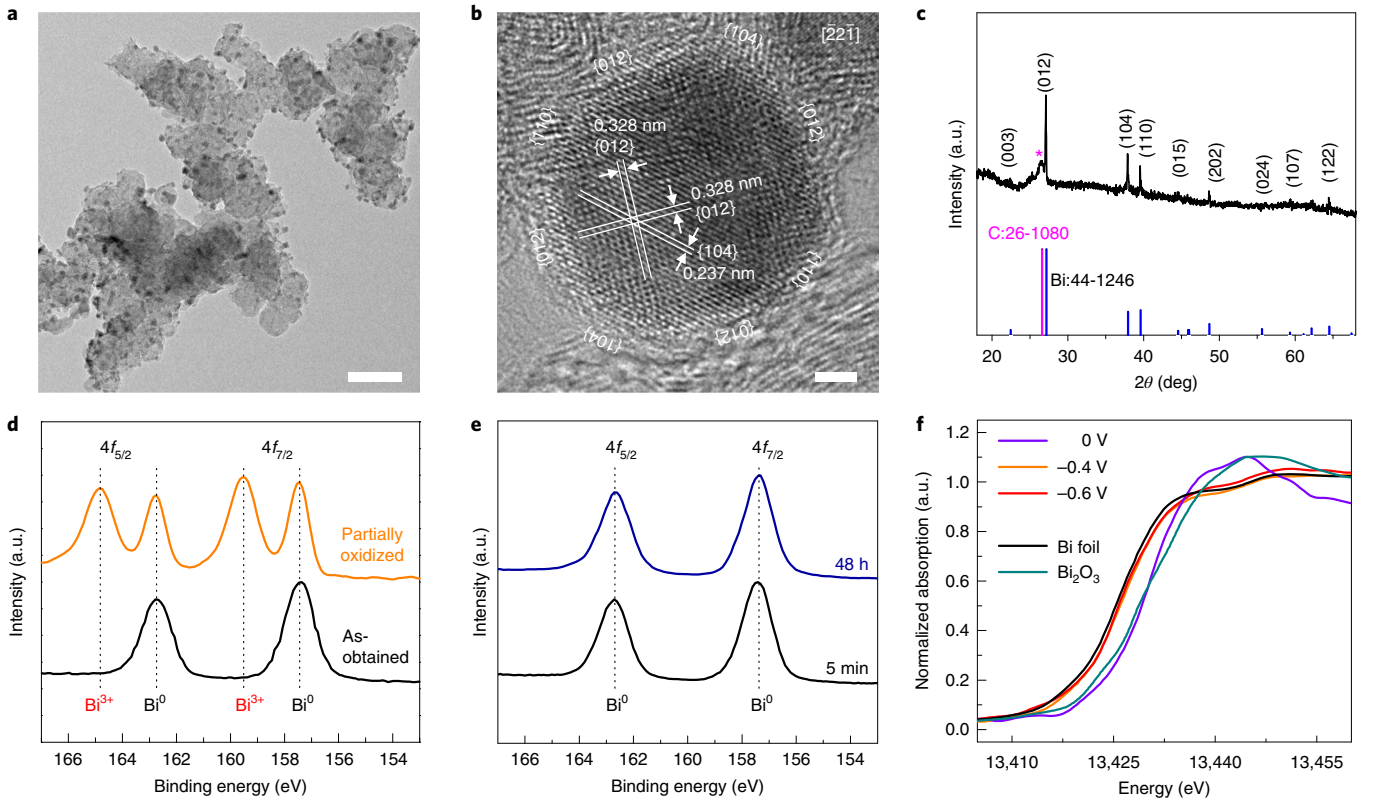

Fig. 2 | Structure, morphology and composition characterizations for BiNCs. a, TEM images for the as-obtained BiNCs (supported on carbon black). **b**, HRTEM image for BiNCs, showing the exposed surfaces of {012}, {104} and {110}. The zone axis is [−22−1]. Scale bars, 100 nm (**a**) and 2 nm (**b**). **c**, XRD patterns for BiNCs. The magenta asterisk denotes the diffraction peak for carbon black. **d**, XPS profiles for the as-obtained and partially oxidized BiNCs. **e**, XPS profiles for the BiNCs after 5 min and 48 hours of ENRR. **f**, In situ XANES profiles for BiNCs at different applied cathode potentials during ENRR.

All three bismuth catalysts showed high stability during the electrolysis process. During the 48 h of continuous reactions, BiNCs, BiNPs and BiBPs exhibited steady total current densities (j_T) of about 0.78, 0.33 and 0.16 mA cm^{-2} with Faradaic efficiencies of about 67, 48 and 41% at −0.60 V, respectively (Fig. 3d). Stability tests at other cathode potentials (−0.55 to −0.65 V) also exhibited steady current density and Faradaic efficiency during long-time reactions (Supplementary Fig. 13). No obvious variations in crystal structures, sizes or morphologies for BiNCs were observed during the electrochemical reactions (Supplementary Fig. 14), confirming their high durability under electrocatalytic conditions. The ex situ XPS and in situ XANES profiles both suggested that the active species for the ENRR were zero-valence bismuth elements (Fig. 2e,f). Much higher geometrical-area-normalized ammonia yield (current density) could be provided by BiNCs supported on carbon paper electrodes with higher bismuth loading (258 μg cm^{-2}). At −0.60 V, BiNCs supported on carbon paper electrodes (BiNCs/CP) could offer an ammonia yield (effective current density) of 5.2×10^{-2} mmol cm^{-2} h^{-1} (4.2 mA cm^{-2}) with a Faradaic efficiency of 66% (Supplementary Fig. 15).

Promotion of the ENRR by potassium cations. Nitrogen reduction can be significantly promoted by potassium cations. When the concentration of K^+ in electrolytes was raised from 0.2 to 1.0 mol l^{-1}, the ENRR current density (j_N) increased from 0.14 to 0.50 mA cm^{-2}, whereas the HER current density (j_H) declined from 1.31 to 0.25 mA cm^{-2}, and thus the Faradaic efficiency for ENRR was boosted from 9.8 to 67% (Fig. 4a,b). Further increasing $c(K^+)$ to 1.2 mol l^{-1} slightly increased the Faradaic efficiency to 68%, but the effective current density dropped slightly from 0.50 to 0.49 mA cm^{-2} because the total current density was decreased due to the suppression of proton diffusion by the high concentration of supporting electrolytes[25].

We then compared the ENRR activity and selectivity at different reaction temperatures to estimate the apparent activation energy (E_a) and to evaluate the effects of potassium cations. As shown in Fig. 4c, the ENRR activity and selectivity both exhibited an increasing trend with the reaction temperature. In electrolytes with 1.0 mol l^{-1} of K^+, the Faradaic efficiency and ammonia yield could be increased from 56% and 48.5 mmol g^{-1} h^{-1} at 10 °C to 67% and 65 mmol g^{-1} h^{-1} at 25 °C, and to as high as 73% and 82.4 mmol g^{-1} h^{-1} at 40 °C. The estimated apparent E_a for the ENRR was 13.7, 21.2 and 30.6 kJ mol^{-1} in electrolytes with 1.0, 0.6 and 0.2 mol l^{-1} of K^+, respectively (Fig. 4d). That is, a high concentration of potassium cations could significantly decrease the apparent E_a and efficiently facilitate the ENRR on BiNCs.

Suppression of the HER by potassium cations. Potassium cations can suppress proton reduction (that is, the HER), the main competing side reaction for the ENRR, on bismuth catalysts in aqueous solutions. HER suppression became even stronger in electrolytes with higher K^+ concentrations. The HER current density at −0.60 V versus RHE can be reduced from 1.32 to 0.56 mA cm^{-2} in Ar-saturated electrolytes (Supplementary Fig. 16) and from 1.31 to 0.25 mA cm^{-2} in N_2-saturated electrolytes (Fig. 4a) by increasing the potassium concentration from 0.2 to 1.0 mol l^{-1}. The observed HER suppression by potassium cations is ascribed to proton migration from the bulk solution to the electrode surface being retarded by supporting electrolytes (for example, K^+) at high concentrations[25,26]. This retarded proton migration to the catalyst surface may further increase the selectivity of the surface reaction to nitrogen reduction, as will be discussed in detail hereinafter.

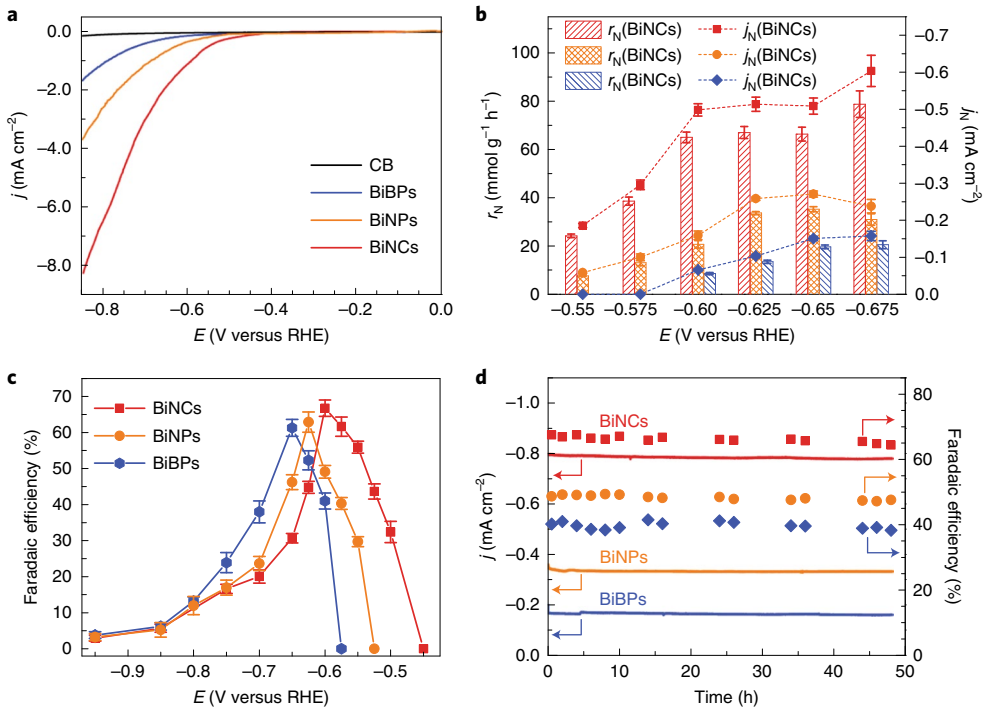

Fig. 3 | ENRR performance for BiNCs, BiNPs and BiBPs in nitrogen-saturated electrolytes (0.5 mol l^{-1} of K_2SO_4, pH 3.5). a, LSV curves for BiNCs, BiNPs, BiBPs and carbon black (CB). Scan rate, 10 mV s^{-1}. **b**,**c**, Effective current densities (j_N, left axis) and ammonia yields (r_N, right axis) (**b**) and (**c**) Faradaic efficiencies for BiNCs, BiNPs and BiBPs at different electrode potentials. Error bars in **b** and **c** indicate the standard deviation of three independent samples. **d**, ENRR activity for BiNCs, BiNPs and BiBPs at −0.60 V versus RHE: total current density (j_T, left axis) and Faradaic efficiency (right axis) versus time.

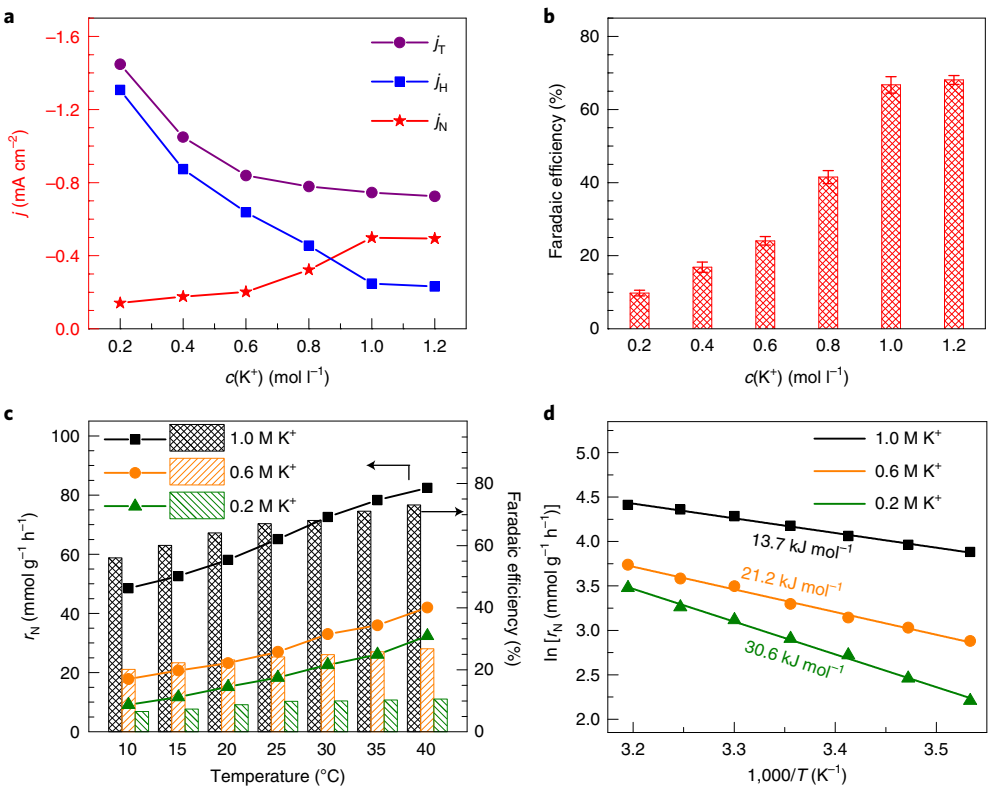

Fig. 4 | Promotion of ENRR on BiNCs by potassium cations (−0.60 V versus RHE, pH 3.5). a, Nitrogen reduction current density (j_N), HER current density (j_H) and total current density (j_T) versus $c(K^+)$. **b**, ENRR Faradaic efficiency versus $c(K^+)$. Error bars represent the standard deviation of three independent samples. **c**, ENRR activity (r_N) and selectivity (Faradaic efficiency) versus different reaction temperatures. $c(K^+) = 1.0$, 0.6 and 0.2 mol l^{-1}. **d**, Apparent activation energy (E_a) for ENRR. $c(K^+) = 1.0$, 0.6 and 0.2 mol l^{-1}.

Promotion of the ENRR on other metals by potassium cations. ENRR promotion and HER suppression by potassium cations also apply to Au and Pt catalysts (Supplementary Figs. 17–21). Au and Pt nanocrystals (denoted AuNCs and PtNCs, Supplementary Figs. 17 and 18) also exhibit increased selectivity and activity for the ENRR in electrolytes containing a high concentration of potassium cations. When the potassium concentration was raised from 0.2 to 1.0 mol l^{-1}, the Faradaic efficiency and effective current density for the ENRR on AuNCs increased from 6.3% and 4.4×10^{-2} mA cm^{-2} to 22.5% and 9.7×10^{-2} mA cm^{-2} (Supplementary Fig. 20). PtNCs, which showed negligible ENRR activity in electrolytes without potassium cations, exhibited a Faradaic efficiency and effective current density of 1.0% and 1.1×10^{-2} mA cm^{-2} with 1.0 mol l^{-1} K^+ (Supplementary Fig. 21). Therefore, potassium cations can generally promote the ENRR on a series of metals (for example, Bi, Au and Pt), among which bismuth exhibits the highest Faradaic efficiency and ammonia yield.

pH effect. The variation in the pH value of electrolytes would also change the ENRR Faradaic efficiency and effective current density, and an optimized pH value of 3.5 was used in our tests (Supplementary Fig. 22). These results suggested that (1) at high pH values (for example, 4.5 to 7) the rate of the ENRR would be limited due to the too limited access to protons for the protonation of nitrogen species and (2) at low pH values (for example, 2.5) competition from the HER would be overwhelming and thus the ENRR would be suppressed.

Thermodynamics for the ENRR on bismuth surfaces. Unlike the Haber–Bosch process at high temperatures, the ENRR, under ambient conditions, would follow the associated mechanisms in which N_2 molecules are reduced and protonated by electrons and protons step by step[10,11]. On metals with relatively weak *N adsorptions (for example, Pt, Au and Ag), the PDS for the ENRR is the reductive protonation of N_2 to *NNH[10,11]. Competition between the adsorptions of nitrogen and hydrogen would dominate the surface reaction selectivity, and the ENRR could be promoted by strengthening the catalyst's affinity to *NNH and/or making the surface adsorption process more selective to *NNH[27].

There are two pathways for the associative nitrogen reduction mechanisms, the distal and alternative pathways. Theoretically, the distal pathway would be more favourable because higher energy barriers are expected for the alternative pathway[10,11]. Experimentally, a considerable amount of N_2H_4 is often detected if the two nitrogen atoms are protonated alternatively[28]. In our experiments, only a trace amount of N_2H_4 (<3%) could be found (Supplementary Fig. 11), suggesting that the distal pathway may be more favourable on bismuth surfaces. Therefore, we performed density functional theory (DFT) computations to depict the thermodynamics for the distal pathway of the associative nitrogen reduction and to calculate the adsorption free energies for the intermediates on Bi(012), (110) and (104) surfaces with/without surface-adsorbed potassium cations (Supplementary Figs. 23 and 24 and Supplementary Table 3).

Simulation results reveal that the PDS for the ENRR on these bismuth surfaces is also the reductive protonation of N_2 to *NNH ($* + N_2 + H^+ + e^- \rightarrow$ *NNH). The nitrogen reduction activity should be dependent on the free-energy change (ΔG_{*NNH}) required for the formation of *NNH. On bare Bi(012), (110) and (104) facets, ΔG_{*NNH} is 3.01, 2.80 and 2.74 eV (at 0 V versus SHE, pH 0), respectively, while ΔG_{*NNH} on a bare Au(111) facet is 3.23 eV, which is at least 0.22 eV higher than that required on bismuth surfaces (Supplementary Fig. 24a). Explicit water molecules were then added in the simulation to include the effects of solvation (Supplementary Figs. 25 and 26)[29,30]. The presence of water could help stabilize the *NNH species on the Bi(012) facet and lower the corresponding ΔG_{*NNH} value to 2.88 eV, while the values on the Bi(110) and (104) facets are almost unchanged (Fig. 5a–c and Supplementary Fig. 24). In comparison, ΔG_{*NNH} on a solvated Au(111) surface is 3.08 eV (Supplementary Fig. 24b), still evidently higher than the values on bismuth surfaces, suggesting better ENRR activity on bismuth surfaces than on the Au(111) surface.

The higher ENRR activity and selectivity on bismuth than on gold can be considered from the point of view of two aspects. First, the *NNH species binds more strongly to bismuth surfaces than to the gold surface, as revealed by the projected density of states (pDOS) of *NNH. The Bi 6*p* bands and the N_{ads} (the N atom directly bonded to the surface) 2*p* orbitals overlap both below and above the Fermi level (Fig. 5d and Supplementary Fig. 27), while the Au 5*d* band has little overlap with the N_{ads} 2*p* orbital (Fig. 5e and Supplementary Fig. 28). The stronger bonding between *NNH and bismuth can be further understood by projected crystal orbital Hamilton populations (pCOHP) analyses[31–35]. For instance, the antibonding orbitals of Bi–N_{ads} on the Bi(012) surface are less occupied than that of Au–N_{ads} on the Au(111) surface (Fig. 5d,e). The integrated pCOHP values up to the Fermi level for Bi–N_{ads} and Au–N_{ads} are −1.09 and −0.66, respectively, suggesting a stronger bonding interaction between N_{ads} and the bismuth surfaces. Bader charges also reflect more electrons donated to the *NNH species from the bismuth surfaces than that from the gold surface (Supplementary Fig. 29). Therefore, stronger interactions between *NNH and the Bi surfaces could stabilize the adsorbates, reduce the energy barriers of the PDS and thus enhance the ENRR activity. Second, nitrogen reduction selectivity will be higher on bismuth than on gold because bismuth is considered an HER poisoner[36–38]. In our simulation, Bader charge analyses indicate that hydrogen atoms would be negatively charged on bismuth but neutrally charged on a gold surface (Supplementary Fig. 30). The neutrally charged hydrogen atoms would be more easily combined to produce H_2 molecules. As a consequence, the stronger ENRR but weaker HER tendency of bismuth over gold contribute to the higher ENRR activity and selectivity on bismuth than on gold catalysts.

Promotion of surface-adsorbed potassium cations. The ENRR activity of bismuth could be significantly enhanced by potassium cations. As shown in Fig. 5a–c, surface-adsorbed potassium cations further decrease the ΔG_{*NNH} from 2.88 to 2.42 eV on the Bi(012) facet and from 2.80 to 2.63 eV on the Bi(110) surface, although there is a slightly raised ΔG_{*NNH} by 0.02 to 2.75 eV on the Bi(104) surface. The pDOS and Bader charges of *NNH can provide additional evidence for potassium's promotion effect (Supplementary Figs. 27–31). In the presence of potassium, the N_{ads} 2*p* orbitals are shifted to lower energies (Supplementary Fig. 27), suggesting the even stronger acceptor character of *NNH in the presence of potassium cations. Potassium can change the surface electronic structures of bismuth (Supplementary Fig. 31). More electrons can be transferred to the *NNH (Supplementary Fig. 29) and stronger Bi–N bonds will be formed. As a result, the N–N bonds are elongated, suggesting better N–N activation on bismuth surfaces in the presence of potassium cations.

In short, our simulations agree with experiments in showing that bismuth catalysts exhibit higher intrinsic nitrogen reduction properties than typical transition-metal catalysts (for example, Au). Surface-adsorbed potassium cations can strengthen the interactions between *NNH species and bismuth surfaces, significantly reduce ΔG_{*NNH} on Bi(012) and (110) facets, and then promote the ENRR activity on bismuth catalysts. It should be acknowledged that, although K^+ promotion and the higher activity of Bi over Au have been clearly elucidated by both simulations and experiments, there are still differences between the calculated PDS barriers and the experimentally observed limiting potentials. Such gaps between the experimental findings and theoretical treatments are often present[1], especially when the supported nanoparticles are modelled by extended surfaces[39]. We hope that more accurate results

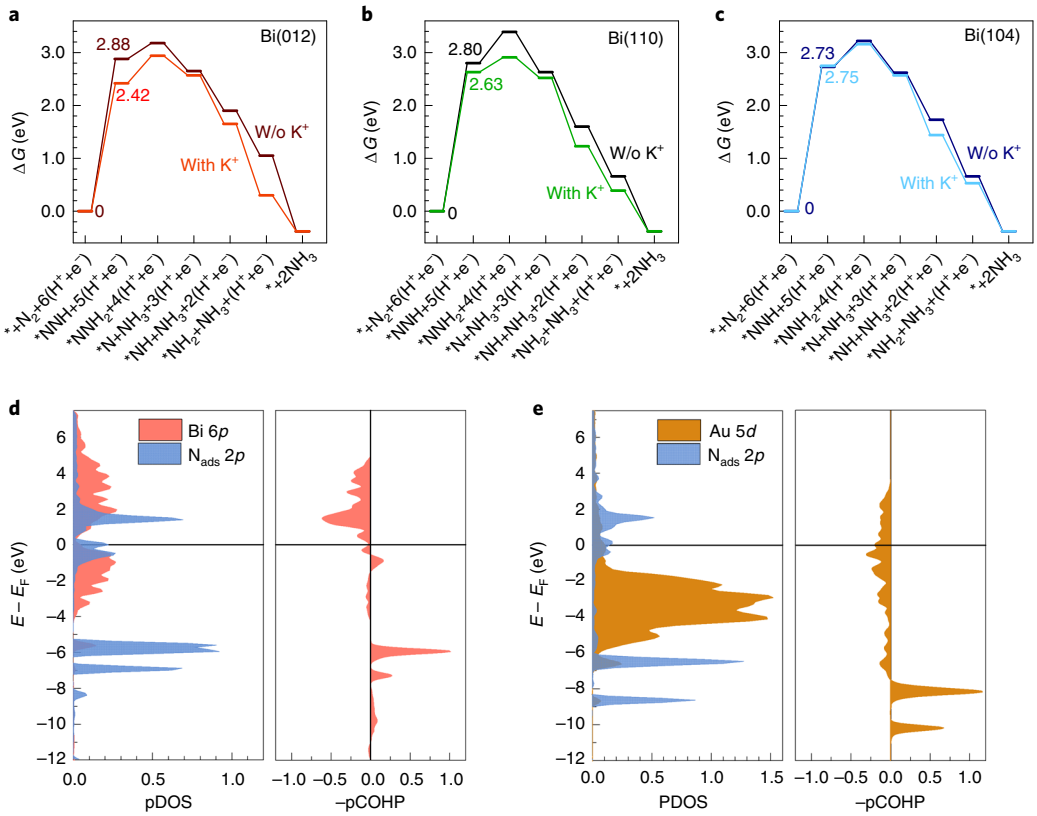

Fig. 5 | Thermodynamics for ENRR on solvated Bi surfaces under conditions with and without K^+. a–c, Gibbs free-energy diagrams of the electrochemical reduction of N_2 to NH_3 on Bi(012) (**a**), (110) (**b**) and (104) (**c**) facets in the presence or absence of K^+ cations (pH 0 and $U = 0$ V versus SHE). **d**,**e**, Projected density of states (pDOS) and projected crystal orbital Hamilton populations (pCOHP) for the N atoms of *NNH directly bonded to the metal atoms (N_{ads}) on Bi(012) (**d**) and Au(111) (**e**) surfaces.

can be obtained with more comprehensive modelling strategies for the reaction energetics with the future development of computation methods.

Further improving ENRR selectivity by suppressing HER. Theoretically, ENRR selectivity and activity can be further promoted by slowing down the transfer of protons to the catalytic surface and making the surface adsorption more selective to nitrogen species[27]. In the microscopic view, after the desorption of products (for example, NH_3 or H_2), the active sites can be occupied by N_2 to form $*N_2$ or by protons to form *H (ref. [27]). If there are sufficient protons in the vicinity of the active sites, hydrogen adsorptions will dominate on most metal surfaces. The HER will occur, and the ENRR will be suppressed. If there are insufficient or even no protons but substantial N_2 molecules around, N_2 will be adsorbed. The ENRR will proceed when additional protons arrive and attack the $*N_2$ adsorbates. Therefore, in theory, ENRR could be promoted by slowing down the proton transfer from the bulk solution to the catalyst surface.

Potassium cations can significantly suppress HER (Fig. 4a and Supplementary Fig. 16) by slowing proton transfer from the bulk solution to the electrode surface[25,26]. Proton migration from the bulk solution to the electrode surface could be retarded by high-concentration supporting cations (for example, K^+)[25,26]. Large amounts of (hydrated) K^+ would be concentrated in the diffusion layer near the surface at low potential[25,29,30,40], and proton transfer through the double layer to the catalytic surface would be slowed[41,42]. In particular, when the proton transfer is hindered such that it is slower than the surface reactions (that is, proton transfer is the rate-limiting step), the protons in the vicinity of the catalyst surface will be depleted. As a result, nitrogen molecules will be adsorbed preferentially to the active sites because nearby protons have been depleted. After the active sites have been occupied by nitrogen, the additional protons diffused from the bulk solution thereafter will attack the $*N_2$ species, and the ENRR will occur. If this scenario happens on most surface sites and proceeds repeatedly, the selectivity for nitrogen reduction will be significantly boosted, and the surface reaction could be dominated by the ENRR (that is, Faradaic efficiency > 50%), even in aqueous solutions. In this study, the ENRR selectivity (Faradaic efficiency) on Au could be increased to 22.5%, which is the highest reported selectivity for ENRR on Au catalysts (Supplementary Table 4). On BiNCs, which exhibit better intrinsic ENRR properties than AuNCs, the Faradaic efficiency can be promoted to a record-high value of ~66–67% as compared to previously reported electrocatalysts under ambient conditions in both aqueous and non-aqueous electrolytes (Supplementary Table 4).

In short, promoted by K^+ ions, BiNCs can exhibit an extraordinarily high ENRR performance in aqueous solutions with a Faradaic efficiency of about 66% and an effective current density of 4.2 mA cm^{-2} under ambient conditions. The mass-normalized ammonia yield (200 mmol g^{-1} h^{-1}) is more than 140 times higher than that on Au catalysts (~1.3–1.4 mmol g^{-1} h^{-1}) in aqueous solutions[18,19] and 1,600 times higher than that on Fe catalysts (0.12 mmol g^{-1} h^{-1}) in ionic liquid electrolytes[23] (Supplementary Fig. 32 and Supplementary Table 4). The Faradaic efficiency (~66–67% at 25 °C and 73% at 40 °C) is close to the optimal value (75%) for enzymatic nitrogen fixation on MoFe nitrogenase[29,30]. The ENRR selectivity (~66%) and activity (0.052 mmol cm^{-2} h^{-1}) either exceed or are very close to the metrics (Faradaic efficiency ≥ 50%, $r_N \geq 0.36$ mmol cm^{-2} h^{-1}) required for possible practical applications[2].

This strategy may expand the library of catalysts and electrolytes for selectively reducing stable molecules (for example, N_2 and CO_2) and find wider applicability in electrochemical systems where the HER should be particularly suppressed. Our extended work suggests that alkali-metal cations (for example, Li^+, Na^+, K^+ and Cs^+) could generally promote the ENRR; among these, K^+ exhibited the best ENRR-promoting effects (Supplementary Fig. 33). In addition, we also found that potassium's promoting effect could be applied to CO_2 reduction under similar conditions (Supplementary Fig. 34). Therefore, it might be a general principle that alkali-metal cations will suppress the HER and promote other PCET reactions on bismuth (and other metals) in aqueous solutions. The differences in the regulating effects of the alkali-metal cations may arise from their different ionic radii (r), charge-to-radius ratios (z/r), hydration energies, hydrated radii and mobility values, among other factors. Further work to determine the mechanism for such general effects is still in progress in our laboratory.

Conclusions

Our strategy shows how to promote ENRR selectivity and activity by modulating the reaction thermodynamics at the surface and regulating the proton transfer process in the electrolyte. Our results suggest that main group metals (p metals) may exhibit much higher ENRR selectivity and activity than the intensively studied transition metals (d metals) due to the stronger interactions between the p orbitals of metal substrates and nitrogen absorbers. We also show that potassium (and other alkali-metal) cations could promote PCET reactions by stabilizing key intermediates and regulating proton transfer from the bulk solution to the catalyst surface, even in aqueous solutions with a substantial number of protons. Following this strategy, future studies may find electrocatalytic systems with even higher ENRR performance by systematically evaluating new catalyst candidates, promoters and/or electrolytes.

In summary, our design represents a successful effort to electrochemically produce ammonia from nitrogen and water with both high selectivity and yield in aqueous solutions under ambient conditions. This discovery may allow the ENRR to compete more favourably with the thermochemical ammonia synthesis processes. These catalysts could be prepared with low cost due to the high abundance and low price of bismuth metals. Electrochemical devices can easily be scaled for ammonia production on demand. With renewable energy as the power input, our method represents an efficient, distributed and sustainable ammonia synthesis route from nitrogen and water with broad scientific and technical impacts.

Methods

Preparation of BiNCs, BiNPs and BiBPs. To prepare BiNCs, 10 mg of carbon black (acetylene, 99.9+%, Alfa Aesar) was fully dispersed in 10 ml of anhydrous ethylene glycol (99%, Alfa Aesar) and sonicated for 2 h before the addition of 5 ml of ethylene glycol solution of 2.8 mM $Bi(NO_3)_3{\cdot}5H_2O$ (98%, Alfa Aesar). The mixture solution was then vigorously stirred for 12 h, sonicated for another 15 min and then transferred to a 25 ml Teflon-lined stainless-steel autoclave. After solvothermal reaction at 180 °C for 16 h, the final product was collected by centrifuge, washed with ethanol several times and then dried under vacuum. The synthesis of BiNPs was similar to that for BiNCs, except that the reaction temperature was set to 200 °C and the reaction time was elongated to 36 h. To synthesize BiBPs, 15 ml of ethylene glycol solution of 0.1 M $Bi(NO_3)_3{\cdot}5H_2O$ was sonicated for 15 min and then transferred to a 25 ml Teflon-lined stainless-steel autoclave for solvothermal reaction at 180 °C for 16 h. The final product was collected by centrifuge, washed with ethanol several times and dried under vacuum. The BiBPs were supported by carbon black before electrocatalytic tests.

Preparation of AuNCs and PtNCs. Carbon black (10 mg) was fully dispersed in 10 ml of anhydrous ethylene glycol and sonicated for ~2 h. Then, 5 ml of ethylene glycol solution of 3.0 mM $HAuCl_4$ or 3.1 mM K_2PtCl_4 was added, respectively, for AuNCs and PtNCs. The mixture solution was then vigorously stirred at room temperature for 12 h and sonicated for another 15 min. After that, 5 ml of ethanol solution of 0.1 M $NaBH_4$ was injected into the mixture solution dropwise under vigorous stirring (1,500 r.p.m.). After another 1 h of continuous stirring, the final product was collected by centrifuge, washed with ethanol and water several times, and finally dried under vacuum.

Material characterizations. XRD was performed on a Rigaku MiniFlex 600 diffractometer with a Cu–Kα X-ray radiation source ($\lambda = 0.154056$ nm) at a scan rate of 6° min^{-1}. XPS measurements were performed on a Thermo VG ESCALAB-250 system with the Al–Kα and Mg–Kα sources operated at 15 kV. TEM and HRTEM studies were performed on JEM-2100 and JEM-2100F (JEOL) transmission electron microscopes operating at 200 kV.

Electrochemical experiment. Electrochemical measurements were carried out in a standard three-electrode H-cell electrochemical system with the cathode and anode components separated by a Nafion 115 membrane (DuPont). A platinum plate (1 × 1 cm^2), an SCE and modified glassy carbon were used as the counter-, reference and working electrode, respectively. All potentials in this study were measured against the SCE and converted to the RHE reference scale by E(V versus RHE) = E(V versus SCE) + 0.0591 × pH + 0.244. Before tests, the Nafion 115 membrane was pretreated in boiled 5% H_2O_2 solution for ~1 h, then in boiled 0.5 M H_2SO_4 solution for another 1 h and finally washed with deionized water several times.

To prepare working electrodes, 13 mg of catalyst (containing 10 mg of carbon black and 3 mg of metal catalyst) was dispersed in a mixed solution of 2 ml of water, 0.7 ml of ethanol and 0.3 ml of 5 wt% Nafion by sonication for at least 30 min to form a homogeneous ink. Then, 12 µl of the as-prepared catalyst ink was loaded onto a glassy carbon electrode (4 mm in diameter).

The pristine electrolyte was prepared using ultrapure water (18 MΩ cm), sulfuric acid and potassium sulfate. The pH value for each electrolyte was adjusted to 3.5 unless especially noted. Before electrolysis, the electrolyte solution was purged with high-purity N_2 (99.999%) for at least 30 min to ensure the removal of residual air in the reaction system. During electrolysis, high-purity N_2 was continuously fed into the cathodic compartment with magnetic stirring (1,200 r.p.m.). For comparison, electrolysis tests were also conducted in high-purity (99.999%) Ar-saturated electrolyte solutions under same experimental conditions. All current densities were normalized to the geometrical area of the electrodes or to the mass of metal catalysts.

Faradaic efficiency calculation. The Faradic efficiency of N_2 reduction (FE_N) was measured based on the definition

$$FE_N = \frac{Q_N}{Q_T} \times 100\% \quad (1)$$

where Q_T and Q_N can be obtained from

$$Q_T = \int_0^t I(t)\,dt \quad (2)$$

$$Q_N = 3 \times n_N \times F \quad (3)$$

and n_N is the amount of the produced ammonia (in moles), F is the Faradaic constant (96,485 C mol^{-1}), I is the reduction current and t is the total reaction time for nitrogen reduction.

TOF estimation. TEM images and the size-distribution histograms for the as-obtained nanoparticles were used to estimate their accessible surface areas and surface atom numbers. We used the sphere model to estimate the accessible surface area (S_A, $m^2\,g^{-1}$) and the number of surface sites (N_{sas}, g^{-1}) from the following equations:

$$S_A = \frac{S}{M} = \frac{4\pi R^2}{\rho \times \frac{4}{3}\pi R^3} = \frac{3}{\rho R} (m^2 g^{-1}) \quad (4)$$

$$N_{sas} = \frac{S_A}{s_{sas}} = \frac{3/\rho R}{\pi r^2} = \frac{3}{\rho \pi R r^2} (g^{-1}) \quad (5)$$

where S, M and R denote the surface area (in m^2), mass (in g) and radius (in m) of the sphere model, r denotes the atomic radius (in m) of the metal atom and ρ denotes the metal density (in $g\,m^{-3}$).

The TOF value of the electrocatalyst is calculated by

$$TOF(h^{-1}) = \frac{r_N \times N_A / 1,000}{N_{sas}} \quad (6)$$

where TOF is the turnover frequency (in h^{-1}), r_N is the ammonia-producing rate (in mmol $g^{-1}\,h^{-1}$), N_A is the Avogadro constant (6.023×10^{23} mol^{-1}) and N_{sas} is the number of surface sites (in g^{-1}).

Quantification of NH_3 with Nessler's reagent, ammonia kit and NMR. The quantity of ammonia produced was measured using a colorimetric method with Nessler's reagent[28]. All test solutions were incubated under dark conditions at 25 °C for 20 min before UV–vis tests. The absorbance at 420 nm for each solution was measured with a UV–vis spectrophotometer (Shimadzu, UV-2600). A series of reference solutions with suitable NH_4Cl concentration was created to plot a calibration curve (Supplementary Fig. 6). The concentrations of ammonia in the electrolytes were obtained with this as-obtained calibration curve.

The amount of ammonia produced was also measured by an enzymatic ammonia assay kit (Sigma-Aldrich). The test procedure followed the standard operation procedure provided by the vendor. Briefly, 100 µl of the resultant electrolyte was first mixed with 1.0 ml of the ammonia assay reagent and incubated in the dark at 25 °C for 5 min. The absorbance at 340 nm for the mixture solution was then measured. After that, 10 µl of L-glutamate dehydrogenase solution (G2294) was added into the solution, and the absorbance at 340 nm was measured again after 5 min of the coloration reaction at 25 °C. The concentrations of ammonia could be calculated with the formulae provided by the assay kit.

To quantify the amount of ammonia by NMR spectroscopy, a certain amount of aliquot (3 ml) was extracted from the electrochemical cell after the ENRR and then mixed with 20% DMSO-d_6 (0.1 ml, Sigma). NMR measurements were then performed on a Bruker Ascend 700 MHz system.

Isotope-labelled experiments. NMR spectra for a series of reference solutions with suitable $^{15}NH_4Cl$ concentrations (10, 20, 30, 50 and 70 µM) were acquired and a calibration curve (ammonium concentration versus ^1H NMR signal at 6.99 ppm) was plotted (Supplementary Fig. 9). The ENRR was performed with $^{15}N_2$ as the gas reactant, and NMR measurements were carried out following a similar procedure as for the reference solutions. The concentration of ammonia in the electrolytes can be obtained from the as-obtained calibration curve.

Quantification of by-products H_2 and N_2H_4. H_2 generated by the HER during electrolysis was measured by online gas chromatography (Shimadzu GC-2014C) with a packed column (MS-13X) and a thermal conductivity detector (TCD). Hydrazine in the electrolyte was measured by the Watt and Chrisp method[43]. Typically, a mixture solution of hydrochloric acid (concentrated, 30 ml), ethanol (300 ml) and para-(dimethylamino) benzaldehyde (5.99 g) was used as the colour reagent. A series of reference solutions with suitable $N_2H_4{\cdot}H_2O$ concentrations was created to measure their UV–vis absorbance at 460 nm and to plot a calibration curve (Supplementary Fig. 6). After the ENRR experiments, 3 ml of electrolyte was pipetted out and mixed with 3 ml of the above as-prepared colour reagent. The mixture solution was incubated in the dark at 25 °C for 20 min before UV–vis adsorption tests. The hydrazine concentration in the electrolytes was obtained from the as-obtained calibration curve.

In situ X-ray absorption fine spectroscopy. In situ XANES data were obtained on the BL14W1 beamline of Shanghai Synchrotron Radiation Facility. The spectra were obtained from 13,400 to 13,480 eV in solid-state detector mode in 0.5 eV steps at the near edge. The ENRR experiments were conducted in a standard three-electrode H-cell. The working electrode were prepared by loading the catalysts on carbon paper, and then fixed and sealed by Kapton films (Supplementary Fig. 4). Chronoamperometry processes at 0, −0.4 and −0.6 V versus RHE were conducted to monitor the valence of the bismuth species. Bismuth foil and Bi_2O_3 powders were used as references.

First-principle calculations. DFT calculations were performed with the Vienna ab initio simulation package (VASP)[44]. The exchange-correlation energy functional was described in the revised Perdew–Burke–Ernzerhof (RPBE)[45] generalized gradient approximation (GGA) with projector augmented wave (PAW) pseudopotentials[46]. The kinetic cutoff energy was 400 eV for all calculations. Spin polarization and dipole corrections were included. The bulk rhombohedral bismuth structure was first optimized, giving lattice parameters of $a = 4.904$ Å and $\alpha = 56.28°$, comparable to the experimental values of $a = 4.746$ Å and $\alpha = 57.24°$ (ref. [47]). The Bi(012) surface was modelled with a periodically repeating (2 × 2) three-layer supercell in which the bottom layer was fixed, while the (104) and (110) surfaces were modelled with (2 × 2) six-layer supercells where the two bottom layers were fixed (Supplementary Fig. 23). For the Au(111) surface, a (4 × 2) three-layer supercell was built with the bottom layer fixed. 20 Å vacuum layers were added to the metal slabs. A (4 × 4 × 1) Monkhorst–Pack k-point sampling was used for the surfaces[48]. Each structure was relaxed until the residual force was smaller than 0.02 eV Å^{-1}. To include the solvation effect, the water coverage was set to 0.5 and four water molecules were added to the metal slabs one by one[29,30], with each geometry optimized. One potassium atom was also added to each of the bismuth and gold slabs to calculate the thermodynamic influence of potassium cations[40]. Atomic charges were calculated according to the atom-in-molecule scheme proposed by Bader[49]. Chemical-bonding analyses were carried out with the computer program LOBSTER (Local Orbitals Basis Suite Towards Electronic-Structure Reconstruction)[31–35].

The elementary steps involved in the thermochemistry of ENRR in acidic condition are as follows:

$$N_2 + H^+ + e^- + * \rightarrow *NNH \quad (7)$$

$$*NNH + H^+ + e^- \rightarrow *NNH_2 \quad (8)$$

$$*NNH_2 + H^+ + e^- \rightarrow *N + NH_3 \quad (9)$$

$$*N + H^+ + e^- \rightarrow *NH \quad (10)$$

$$*NH + H^+ + e^- \rightarrow *NH_2 \quad (11)$$

$$*NH_2 + H^+ + e^- \rightarrow NH_3 + * \quad (12)$$

Only the associative distal pathway was considered in this work, because the energetics have been shown to be more favoured in this reaction mechanism[10,11,50].

To calculate the Gibbs energy change of each elementary step, the potential of the SHE was set as the reference potential, in which the chemical potential of the $(H^+ + e^-)$ pair was related to half of the chemical potential of hydrogen (H_2) at pH 0 (ref. [51]). For each step, $\Delta G = \Delta E - T\Delta S + \Delta E_{ZPE} + \Delta G_U + \Delta G_{pH}$. ΔE denotes the reaction energy. ΔS and ΔE_{ZPE} are the changes in entropy and zero-point energy, respectively, and were computed from the vibrational frequencies of the adsorbed species; the corresponding values of the gas-phase molecules were taken from the NIST database. ΔG_U represents the effect of applied bias and is equal to $-neU$, in which n is the number of transferred electrons in each step. ΔG_{pH} is the contribution of H^+ and is equal to $-k_B T \times \ln(10) \times pH$, where k_B is the Boltzmann constant. To produce thermodynamic values comparable to those of other works, the free energy at 0 V versus SHE (pH 0) was computed. The adsorption free energies for the ENRR intermediates are listed in Supplementary Table 3. The atomic coordinates of the optimized models for NNH adsorption are provided in the Supplementary Information.

Data availability

The data that support the findings of this study are available from the corresponding author upon reasonable request.

Received: 25 June 2018; Accepted: 29 January 2019;
Published online: 04 March 2019

References

1. van der Ham, C. J. M., Koper, M. T. M. & Hetterscheid, D. G. H. Challenges in reduction of dinitrogen by proton and electron transfer. *Chem. Soc. Rev.* **43**, 5183–5191 (2014).
2. Kyriakou, V., Garagounis, I., Vasileiou, E., Vourros, A. & Stoukides, M. Progress in the electrochemical synthesis of ammonia. *Catal. Today* **286**, 2–13 (2017).
3. Shipman, M. A. & Symes, M. Recent progress towards the electrosynthesis of ammonia from sustainable resources. *Catal. Today* **286**, 57–68 (2017).
4. Guo, C. X., Ran, J. R., Vasileff, A. & Qiao, S. Z. Rational design of electrocatalysts and photo(electro)catalysts for nitrogen reduction to ammonia (NH_3) under ambient conditions. *Energy Environ. Sci.* **11**, 45–56 (2018).
5. Cao, N. & Zheng, G. F. Aqueous electrocatalytic N_2 reduction under ambient conditions. *Nano Res.* **11**, 2992–3008 (2018).
6. Deng, J., Iñiguez, J. A. & Liu, C. Electrocatalytic nitrogen reduction at low temperature. *Joule* **2**, 846–856 (2018).
7. Chen, J. G. et al. Beyond fossil fuel-driven nitrogen transformations. *Science* **360**, eaar6611 (2018).
8. Ertl, G. Reactions at surfaces: From atoms to complexity. *Angew. Chem. Int. Ed.* **47**, 3524–3535 (2008).
9. Appl, M. in *Ullmann's Encyclopedia of Industrial Chemistry* (Wiley-VCH, Weinheim, 2006).
10. Skúlason, E. et al. A theoretical evaluation of possible transition metal electro catalysts for N_2 reduction. *Phys. Chem. Chem. Phys.* **14**, 1235–1245 (2012).
11. Montoya, J. H., Tsai, C., Vojvodic, A. & Nørskov, J. K. The challenge of electrochemical ammonia synthesis: a new perspective on the role of nitrogen scaling relations. *ChemSusChem* **8**, 2180–2186 (2015).
12. Kordali, V., Kyriacou, G. & Lambrou, Ch. Electrochemical synthesis of ammonia at atmospheric pressure and low temperature in a solid polymer electrolyte cell. *Chem. Commun.* 1673–1674 (2000).
13. Lan, R., Irvine, J. T. S. & Tao, S. W. Synthesis of ammonia directly from air and water at ambient temperature and pressure. *Sci. Rep.* **3**, 1145 (2013).

14. Chen, S. M. et al. Electrocatalytic synthesis of ammonia at room temperature and atmospheric pressure from water and nitrogen on a carbon-nanotube-based electrocatalyst. *Angew. Chem. Int. Ed.* **56**, 2699–2703 (2017).
15. Chen, G. F. et al. Ammonia electrosynthesis with high selectivity under ambient conditions via a Li^+ incorporation strategy. *J. Am. Chem. Soc.* **139**, 9771–9774 (2017).
16. Bao, D. et al. Electrochemical reduction of N_2 under ambient conditions for artificial N_2 fixation and renewable energy storage using N_2/NH_3 cycle. *Adv. Mater.* **29**, 604799 (2017).
17. Li, S. J. et al. Amorphizing of Au nanoparticles by CeO_x–RGO hybrid support towards highly efficient electrocatalyst for N_2 reduction under ambient conditions. *Adv. Mater.* **29**, 1700001 (2017).
18. Shi, M. M. et al. Au sub-nanoclusters on TiO_2 toward highly efficient and selective electrocatalyst for N_2 conversion to NH_3 at ambient conditions. *Adv. Mater.* **29**, 1606550 (2017).
19. Lv, C. D. et al. An amorphous noble-metal-free electrocatalyst that enables nitrogen fixation under ambient conditions. *Angew. Chem. Int. Ed.* **57**, 6073–6076 (2018).
20. Yao, Y., Zhu, S. Q., Wang, H. J., Li, H. & Shao, M. H. A spectroscopic study on the nitrogen electrochemical reduction reaction on gold and platinum surfaces. *J. Am. Chem. Soc.* **140**, 1496–1501 (2018).
21. Wang, J. et al. Ambient ammonia synthesis via palladium-catalyzed electrohydrogenation of dinitrogen at low overpotential. *Nat. Commun.* **9**, 1795 (2018).
22. Kim, K., Yoo, C. Y., Kim, J. N., Yoon, H. C. & Han, J. I. Electrochemical synthesis of ammonia from water and nitrogen in ethylenediamine under ambient temperature and pressure. *J. Electrochem. Soc.* **163**, F1523–F1526 (2016).
23. Zhou, F. L. et al. Electro-synthesis of ammonia from nitrogen at ambient temperature and pressure in ionic liquids. *Energy Environ. Sci.* **10**, 2516–2520 (2017).
24. Lee, H. K. et al. Favoring the unfavored: selective electrochemical nitrogen fixation using a reticular chemistry approach. *Sci. Adv.* **4**, eaar3208 (2018).
25. Bard, A. J. & Faulkner, L. R. *Electrochemical Methods: Fundamentals and Applications* 2nd edn (Wiley, New York, NY, 2001).
26. Mukouyama, Y., Nakazato, R., Shiono, T., Nakanishi, S. J. & Okamoto, H. Potential oscillation during electrolysis of water in acidic solutions under numerous conditions. *J. Electroanal. Chem.* **713**, 39–46 (2014).
27. Singh, A. R. et al. Electrochemical ammonia synthesis—the selectivity challenge. *ACS Catal.* **7**, 706–709 (2017).
28. Li, H., Shang, J., Ai, Z. H. & Zhang, L. Z. Efficient visible light nitrogen fixation with BiOBr nanosheets of oxygen vacancies on the exposed {001} facets. *J. Am. Chem. Soc.* **137**, 6393–6399 (2015).
29. Mills, J. N., McCrum, I. T. & Janik, M. J. Alkali cation specific adsorption onto fcc(111) transition metal electrodes. *Phys. Chem. Chem. Phys.* **16**, 13699–13707 (2014).
30. McCrum, I. T. & Janik, M. J. pH and alkali cation effects on the Pt cyclic voltammogram explained using density functional theory. *J. Phys. Chem. C* **120**, 457–471 (2016).
31. Dronskowski, R. & Blochl, P. E. Crystal orbital Hamilton populations (COHP). Energy-resolved visualization of chemical bonding in solids based on density-functional calculations. *J. Phys. Chem.* **97**, 8617–8624 (1993).
32. Deringer, V. L., Tchougreeff, A. L. & Dronskowski, R. Crystal orbital Hamilton population (COHP) analysis as projected from plane-wave basis sets. *J. Phys. Chem. A* **115**, 5461–5466 (2011).
33. Maintz, S., Deringer, V. L., Tchougreeff, A. L. & Dronskowski, R. Analytic projection from plane-wave and PAW wavefunctions and application to chemical-bonding analysis in solids. *J. Comput. Chem.* **34**, 2557–2567 (2013).
34. Maintz, S., Deringer, V. L., Tchougreeff, A. L. & Dronskowski, R. LOBSTER: a tool to extract chemical bonding from plane-wave based DFT. *J. Comput. Chem.* **37**, 1030–1035 (2016).
35. Maintza, S., Essera, M. & Dronskowski, R. Efficient rotation of local basis functions using real spherical harmonics. *Acta Phys. Pol. B* **47**, 1165–1175 (2016).
36. Trasatti, S. Work function, electronegativity, and electrochemical behaviour of metals: III. Electrolytic hydrogen evolution in acid solutions. *J. Electroanal. Chem.* **39**, 163–184 (1972).
37. Markovi, N. M. & Ross, P. N. Jr Surface science studies of model fuel cell electrocatalysts. *Surf. Sci. Rep.* **45**, 117–229 (2002).
38. Greeley, J., Jaramillo, T. F., Bonde, J., Chorkendorff, I. & Nørskov, J. K. Computational high-throughput screening of electrocatalytic materials for hydrogen evolution. *Nat. Mater.* **5**, 909–913 (2006).
39. Nørskov, J. K., Bligaard, T., Rossmeisl, J. & Christensen, C. H. Towards the computational design of solid catalysts. *Nat. Chem.* **1**, 37–46 (2009).
40. Liu, M. et al. Enhanced electrocatalytic CO_2 reduction via field-induced reagent concentration. *Nature* **537**, 382–386 (2016).
41. Ledezma-Yanes, I. et al. Interfacial water reorganization as a pH-dependent descriptor of the hydrogen evolution rate on platinum electrodes. *Nat. Energy* **2**, 17031 (2017).
42. Chen, X., McCrum, I. T., Schwarz, K. A., Janik, M. J. & Koper, M. T. M. Co-adsorption of cations as the cause of the apparent pH dependence of hydrogen adsorption on a stepped platinum single-crystal electrode. *Angew. Chem. Int. Ed.* **56**, 15025–15029 (2017).
43. Watt, G. W. & Chrisp, J. D. Spectrophotometric method for determination of hydrazine. *Anal. Chem.* **24**, 2006–2008 (1952).
44. Hafner, J. Ab-initio simulations of materials using VASP: density-functional theory and beyond. *J. Comput. Chem.* **29**, 2044–2078 (2008).
45. Hammer, B., Hansen, L. & Nørskov, J. Improved adsorption energetics within density-functional theory using revised Perdew–Burke–Ernzerhof functionals. *Phys. Rev. B* **59**, 7413–7421 (1999).
46. Blöchl, P. E. Projector augmented-wave method. *Phys. Rev. B* **50**, 17953–17979 (1994).
47. Barrett, C. S. The structure of bismuth at low temperatures. *Aust. J. Phys.* **13**, 209–222 (1960).
48. Monkhorst, H. J. & Pack, J. D. Special points for Brillouin-zone integrations. *Phys. Rev. B* **13**, 5188–5192 (1976).
49. Bader, R. F. W. A quantum theory of molecular structure and its applications. *Chem. Rev.* **91**, 893–928 (1991).
50. Back, S. & Jung, Y. On the mechanism of electrochemical ammonia synthesis on the Ru catalyst. *Phys. Chem. Chem. Phys.* **18**, 9161–9166 (2016).
51. Nørskov, J. K. et al. Origin of the overpotential for oxygen reduction at a fuel-cell cathode. *J. Phys. Chem. B* **108**, 17886–17892 (2004).

Acknowledgements

The authors thank W. Sun, G. Wang and Z. Zhou for helpful discussions. The authors acknowledge the Analytical and Testing Center of BIT for technical support and the High-Performance Computing Platform of PKU for supporting the computational work. A.X.Y. acknowledges financial support from the National Natural Science Foundation of China (grant no. 21601015) and the Beijing Institute of Technology Research Fund Program for Young Scholars. Y.W.Z. acknowledges financial support from the National Key Research and Development Program of China (no. 2016YFB0701100), the National Natural Science Foundation of China (nos. 21832001, 21771009, 21573005 and 21621061) and the Beijing Natural Science Foundation (no. 2162019). C.H.Y. acknowledges financial support from the National Natural Science Foundation of China (nos. 21331001, 21590791 and 21461162001) and the National Key Research and Development Program of China (nos. 2014CB643800 and 2017YFA0205101).

Author contributions

A.-X.Y., Y.-W.Z. and C.-H.Y. designed the research. Y.-C.H. synthesized the catalysts, conducted the structure analysis and electrocatalytic studies. Y.G., X.-Y.W., Y.-W.Z. and C.-H.Y. performed the DFT calculations. Y.-C.H., L.-W.C., M.S. and R.S. performed the in situ XANES analysis. L.-W.C., Y.G., T.-A.B., W.-Y.G., N.Z., X.S., X.F., J.-W.Z., B.W. and C.-W.H. assisted with material characterizations and catalysis measurements. A.-X.Y., Y.-C.H. and Y.G. co-wrote the paper. A.-X.Y., Y.-W.Z. and C.-H.Y. supervised the research. All authors discussed the results and assisted during manuscript preparation.

Competing interests

The authors declare no competing interests.

Additional information

Supplementary information is available for this paper at https://doi.org/10.1038/s41929-019-0241-7.

Reprints and permissions information is available at www.nature.com/reprints.

Correspondence and requests for materials should be addressed to A.-X.Y., R.S., Y.-W.Z. or C.-H.Y.

Publisher's note: Springer Nature remains neutral with regard to jurisdictional claims in published maps and institutional affiliations.